Supplementary Information (SI) for Energy & Environmental Science.
This journal is © The Royal Society of Chemistry 2025

Supplementary Material (SI) for Energy & Environmental Science.
This journal is © The Royal Society of Chemistry 20XX

Supporting Information

Highly crystalline nitrogen-doped carbon anchored well-distributed Fe_3O_4 nanoparticles for high-efficient neutral H_2O_2 electrosynthesis

Hao Yin [a], Jili Yuan [a]*, Jun Wang [b]*, Shiwei Hu [c]*, Pingshan Wang [b], Haibo Xie[a]*

a. Department of Polymer Materials and Engineering, College of Materials & Metallurgy, Guizhou University, Huaxi District, Guiyang 550025, P.R. China. E-mail: jlyuan@gzu.edu.cn, hbxie@gzu.edu.cn

b. Environmental Research at Greater Bay Area; Key Laboratory for Water Quality and Conservation of the Pearl River Delta, Ministry of Education, Guangzhou University, Guangzhou 510006, China. E-mail: wangjun@gzhu.edu.cn, chemwps@csu.edu.cn

c. Institute of Mechanics, Chinese Academy of Sciences, Beijing, China. E-mail: hushiwei@imech.ac.cn

Experimental Section

Chemicals and Materials

All chemical reagents are analytical grade and used without any further purification. Melamine ($C_3H_6N_6$, 99%), terephthalaldehyde (AR), chloroform ($CHCl_3$, 99.9%) 1,2-Dichloroethane ($C_2H_4Cl_2$, 99.5%), 2-acetylpyridine (AR), Iron (II) chloride tetrahydrate ($FeCl_2 \bullet 4H_2O$, 99%), anhydrous ethanol (C_2H_5OH, 99.9%), dichloromethane (CH_2Cl_2, 99.9%), methanol (CH_3OH, 99%), and sodium sulfate anhydrous (Na_2SO_4, 99%) repurchased from Aladdin (Shanghai, China). Lithium perchlorate ($LiClO_4$, 98%), Hydrogen peroxide (H_2O_2, 30 wt%), and sulfuric acid (H_2SO_4, 95~98%) were purchased from Sinopharm Chemical Reagent Co., Ltd. (China). Nafion solution (D520, 5.0 wt.%), Proton exchange membrane (Nafion 212, 115, and 117), and carbon paper (AvCarb GDS 2230 and Spectracarb 2050A-1050) were purchased from Sci-Materials Hub (http://www.scimaterials.cn/). Ultrapure water ($\geq$18.25 MΩ) is used for the preparation of all aqueous solutions.

Material characterizations

The X-ray powder diffraction (XRD) was performed using a Rigaku Ultima IV X-ray diffractometer equipped with a Cu K radiation source operating at 40 kV and 200 mA. At an excitation wavelength of 532 nm, Raman and in situ Raman spectroscopy spectra were obtained on a Horriba Jovin Yvon LabRam Aramis. On a transmission electron microscope (TEM; FEI-TALOS-F200X) running at an acceleration voltage of 200 kV, the morphological analysis was conducted. X-ray absorption fine structure (XAFS) spectroscopy was carried out using the RapidXAFS 2M (Anhui Absorption Spectroscopy Analysis Instrument Co., Ltd.) by transmission (or fluorescence) mode at 20 kV and 30 mA, and the Si (531) spherically bent crystal analyzer with a radius of curvature of 500 mm was used for Fe. The KBr-disk method was used to prepare the test specimens. The thermogravimetric Fourier transform infrared (TG-FTIR) analyzer consists of a thermogravimetric analyzer TG 209 F1 (Netzsch, Germany) and a Fourier infrared spectrometer FTIR NicoletiS50 (Thermo Fisher Scientific, USA). The specific surface area was determined by the Brunauer-Emmett-Teller (BET) method with N_2 adsorption at 77 K (BELSORP-mini II). Inductively Coupled Plasma-Optical Emission Spectrometry (ICP-OES) was performed using an Agilent 5110 instrument.

Electrochemical ORR measurement

The electrochemical oxygen reduction reaction (ORR) was conducted using a three-electrode configuration with a counter of Pt ring and Ag/AgCl reference electrode on an RRDE setup (AFMSRCE model; disk OD = 5.61 mm; ring OD = 7.91 mm; ring ID = 6.25 mm; Pine Research Instrumentation, USA) and a CHI 760E potentiostat. For the preparation of the working electrode, the catalyst ink was prepared by ultrasonically mixing 1 mg of the catalyst, 0.196 mL of ultra-pure water, 0.196 mL of alcohol, and 8 μL of 5 wt % D520 Nafion dispersion solution and further drop-casting on freshly polished RRDE with a catalyst loading density of 100 μg cm^{-2}. All potentials were transformed to the reversible hydrogen electrode (RHE) after being adjusted for by solution resistance. The polarization curves of ORR were obtained by measuring linear sweep Voltammograms (LSV) with a sweep speed of 5 mV s^{-1} at 1600 rpm in the electrolyte of O_2- or Air-saturated and the Pt ring potential was kept at 1.2 V to respond to the generated H_2O_2. The chronoamperometry measurement was fixed at 0.5 V using 400 rpm for 12 h. The collection efficiency (N) on the RRDE electrode was determined in 1 M KCl +10 mM K_3[Fe(CN) at different rotation speeds, the scanning rate of 50 mV/s in which the potential on disk was scanned from 1.0 V to 0.1 V to reduce Fe^{3+} to Fe^{2+} while the potential on Pt ring was held at 0.5 V to oxidize Fe^{2+} to Fe^{3+}. As a result, the rate of collection efficiency (N) was calculated to be 37.5% (Figure S35). The electrochemically active surface area (ECSA) of the various catalysts was determined by performing cyclic voltammetry (CV) at different scan rates between 0.90V and 1.10 V (without iR-correction) in O_2-saturated electrolyte. The ECSA measurements were run at 25 °C in a customized gastight H-type glass cell separated by Nafion 115 membrane. The working electrode is prepared with carbon paper (GDS2230, 1×1 cm) by coating catalysts with a loading amount of 1 mg cm^{-2}. The H_2O_2 selectivity and transfer number electron (n) were computed using the following formulas based on disk current (I_{Disk}) and ring current (I_{Ring}) data:

$$H_2O_2\% = 200\frac{I_{Ring}/N}{I_{Disk} + I_{Ring}/N} \tag{1}$$

$$n = 4\frac{I_{Disk}}{I_{Disk} + I_{Ring}/N} \tag{2}$$

K-L polt. The kinetic current in Figure 3d and 3f (Tafel and Tafel-A-g) is estimated according to the following Koutecky-Levich equation:

$$\frac{1}{j} = \frac{1}{j_k} + \frac{1}{j_d} = \frac{1}{j_k} + \left(\frac{1}{0.620\, n\, F\, A\, D^{2/3}\, V^{-1/6}\, C}\right)\omega^{-\frac{1}{2}} \tag{3}$$

in which, j is the apparent current, j_k is the kinetic current, n is the number of electrons transferred in reaction, F is the Faraday constant (96485 C/mol), A is the electrode area, 0.2475 cm^2, D is the diffusion coefficient of oxygen, 1.93×10^{-5} cm^2/s, V is the kinematic viscosity of the solution, 0.01 cm^2/s, ω is the angular rotation rate, and C is the concentration of oxygen in the solution, 1.26×10^{-6} mol/cm^3. Kinetic current is estimated at apparent current values corresponding to less than half of the diffusion-limited currents range to avoid large errors.

TOF. The formula for calculating turnover frequency (TOF) is shown below:

$$TOF = \frac{J_k N_e}{\omega_{Fe} C_{cat} N_A / M_{Fe}} \tag{4}$$

where J_k is the kinetic current density (mA cm^{-2}), Ne represents the electron number per Coulomb 6.24×10^{18}, ω_{Fe} is the atomic content of active Fe in Fe_3O_4@TNC (it is considered that t that the Fe atoms on the surface Fe_3O_4 are all active sites of the catalyst), $C_{cat.}$ is the catalyst loading, N_A is the Avogadro constant 6.022×10^{23}, and M_{Fe} is the molar mass of Fe (55.845 g mol^{-1}).

In-situ ATR-FTIR spectrum

The in situ attenuated total reflectance Fourier transform infrared spectroscopy (ATR-FTIR) that uses IRRAS measurement was performed on FTIR (Nicolet iS50, Thermo Fisher Scientific) with an MCT detector. The spectral resolution was 4 cm^{-1} and the scan time was 64 times. The GDS2230 Carbon paper with a catalyst loading of 0.20 mg cm^{-2} was used as the working electrode with the Pt plate and Ag/AgCl electrode being used as the counter and reference electrodes. The in situ FTIR spectra were acquired during the Chronopotentiometry test in O_2-saturated 0.1 M $LiClO_4$ with constant O_2 (20 mL min^{-1}) bubbling into the reaction cell.

In situ Raman characterizations

In this study, in situ Raman measurements were made with a modified electrochemical Raman cell (three-electrode PEEK cell with a 1.5 cm diameter circular quartz window) on the CIS-Raman-EC(S)-U2 (In-situ High-tech) potentiostat. and a confocal Raman spectrometer (Horriba Jovin Yvon LabRam Aramis). As the light source, a 532 nm excitation laser (10%) with a power of 2.1 mW was utilized and focused on the sample surface through a dry objective lens with NA = 0.5 (Olympus, 10X, WD = 10.6 mm). The distance between the quartz window and the working electrode surface is less than 0.1 mm during the Raman measurements, making the solution layer on the working electrode surface very thin, allowing the solution layer's weakening influence on the Raman signal to be as modest as feasible. The catalyst was coated on a 1.5 cm×1.5 cm patch of carbon paper (GDS 2230) to create the working electrode for the in-situ Raman experiments and 1 mg of catalyst ink was equally deposited onto the surface of the carbon paper and dried. Each potential-dependent Raman spectrum presented here was collected over 15 seconds and represents measurements taken after holding each potential between 0.05 and 1.0 V vs RHE for half a minute in either the positive or negative direction.

Determination of the H_2O_2 concentration

A titration process was used to assess the concentration of the produced H_2O_2. Following electrolysis, the H_2O_2 solution was collected and measured using the established potassium permanganate (0.02 M $KMnO_4$ solution, Calibration through sodium oxalate) titration procedure by the following equation:

$$2K\mathit{Mn}O_4 + 5H_2O_2 + 3H_2SO_4 \rightarrow 5O_2\uparrow + 2\mathit{Mn}SO_4 + K_2SO_4 + 8H_2O\cdot\cdot \quad (5)$$

The H^+ source employed was sulfuric acid (1.0 M H_2SO_4). The following equation is used to compute the FE for H_2O_2 production:

$$FE = \frac{\text{generated } H_2O_2\left(\text{mol L}^{-1}\right) \times 2 \times 96485 \times V\ (\text{mL})}{j_{total}\ (\text{mA}) \times t\ (\text{s})} \times 100\%$$

(6)

Figures and Tables

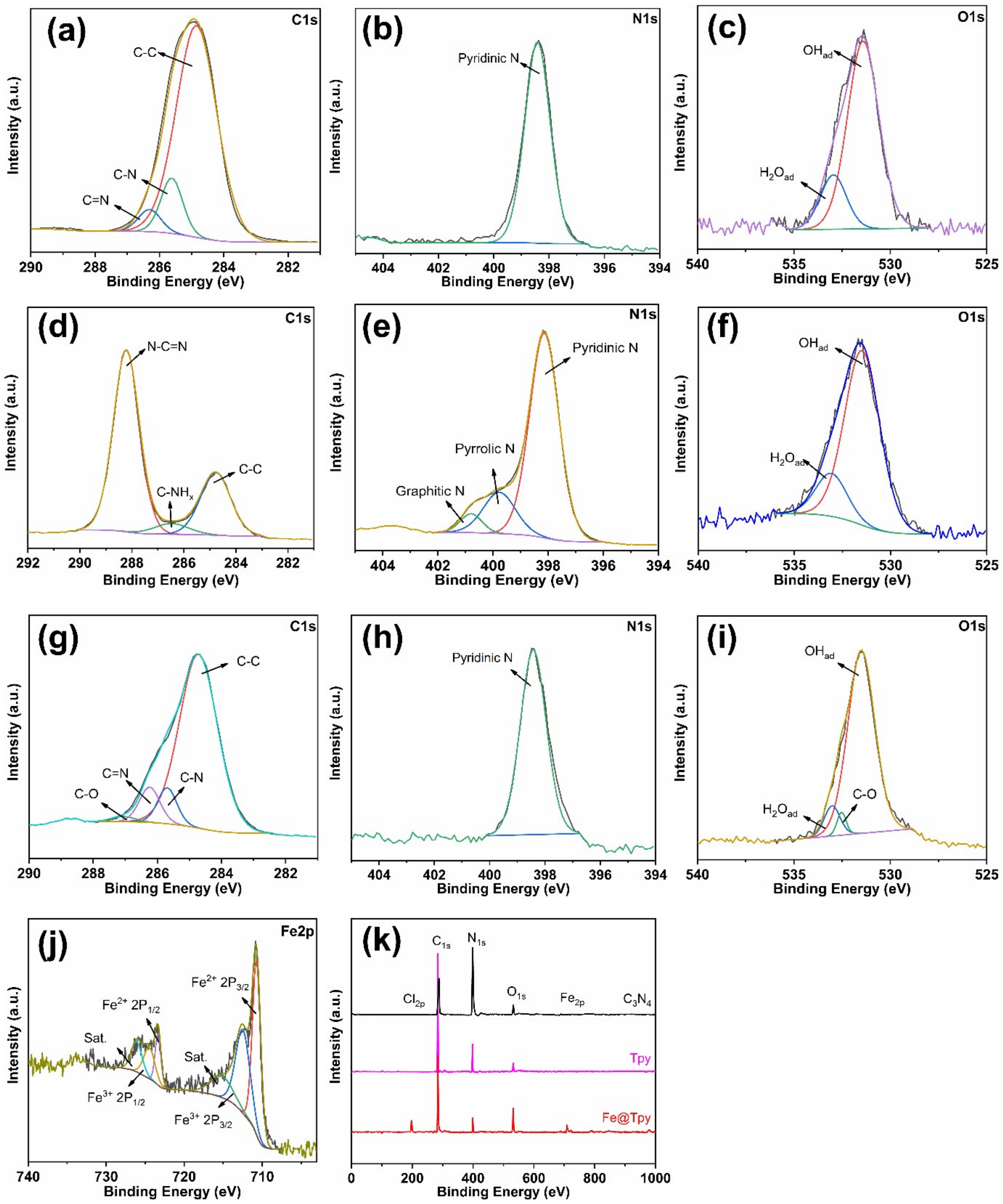

Figure S1. X-ray photoelectron spectra (XPS) of linear bis-terpyridine ligand (Tpy) graphic carbon nitride (g-C_3N_4), and Fe@Tpy. XPS C 1s of (a) Tpy, (d) g-C_3N_4, and (g) Fe@Tpy. XPS N 1s of (b) Tpy, (e) g-C_3N_4, and (h) Fe@Tpy XPS O 1s of (c) Tpy, (f) g-C_3N_4, and (i) Fe@Tpy, and XPS (j) Fe 2p of Fe@Tpy. XPS survey spectra of g-C_3N_4, Tpy, and Fe@Tpy.

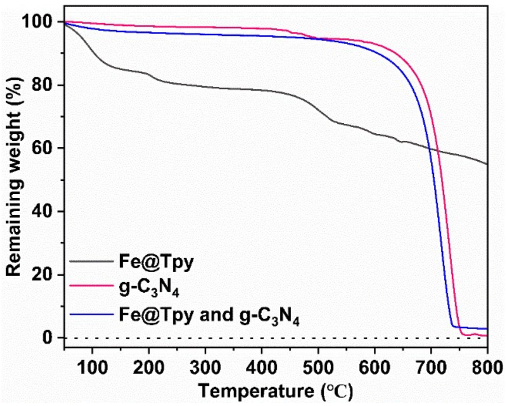

Figure S2. Thermogravimetric curves of the pyrolysis of Fe@Tpy, g-C_3N_4, and the mixture of both Fe@Tpy and g-C_3N_4.

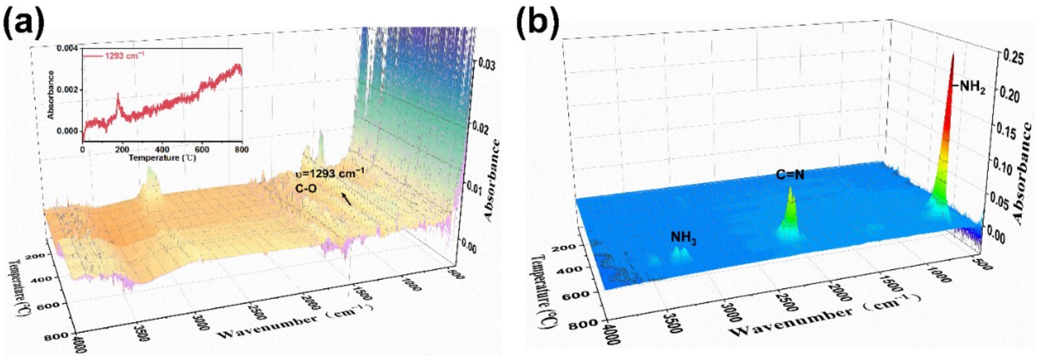

Figure S3. 3D colormap surface of FTIR for the escaping gases of (a) pure Fe@Tpy and (b) the mixture of both Tpy and g-C_3N_4.

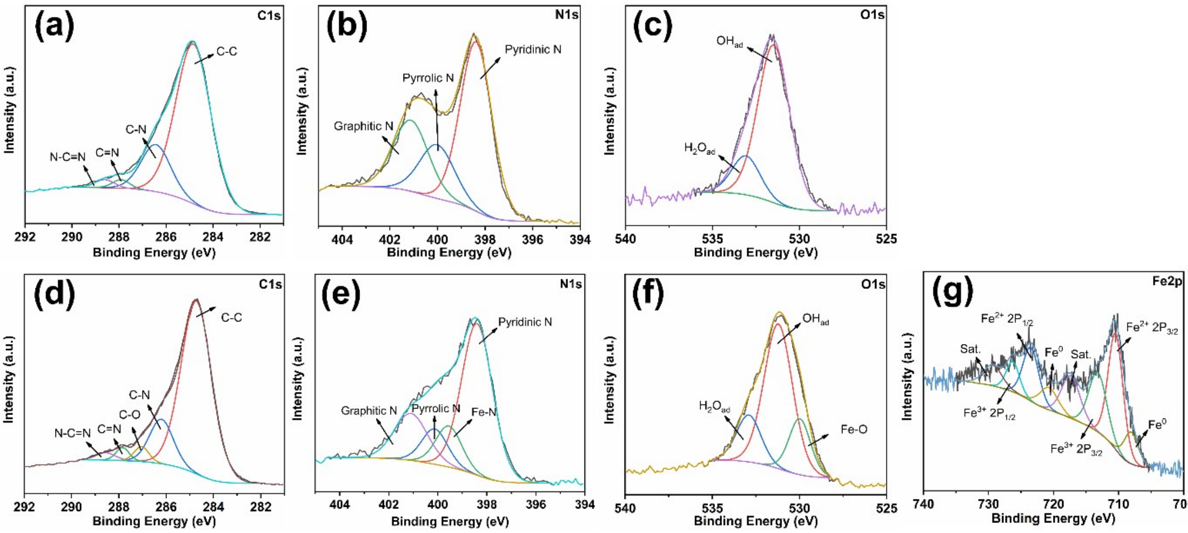

Figure S4. XPS spectrums of TNC and Fe_3O_4@TNC. XPS C 1s of (a) TNC and (d) Fe_3O_4@TNC, N 1s of (b) TNC and (e) Fe_3O_4@TNC, O1s of (c) TNC and (f) Fe_3O_4@TNC, and (g)Fe 2p of Fe_3O_4@TNC.

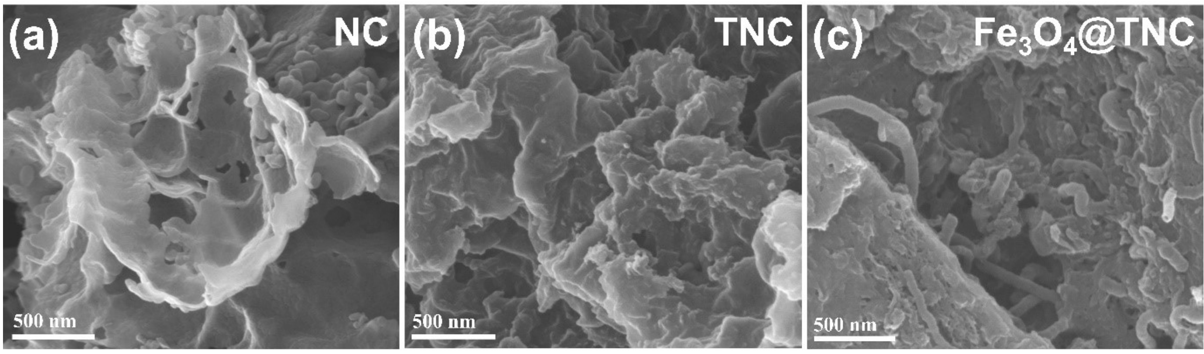

Figure S5. Field emission scanning electronic microscopy (FE-SEM) images of (a) NC, (b) TNC, and (c) Fe_3O_4@TNC.

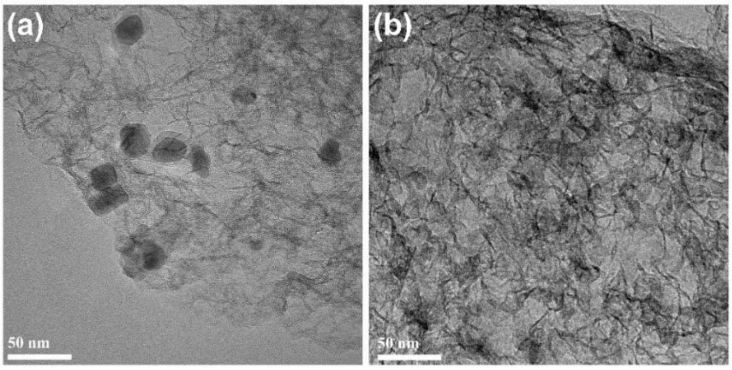

Figure S6. TEM images of (a) Fe_3O_4@TNC and (b) TNC.

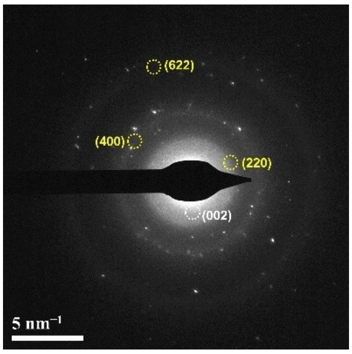

Figure S7. SAED pattern of Fe_3O_4@TNC.

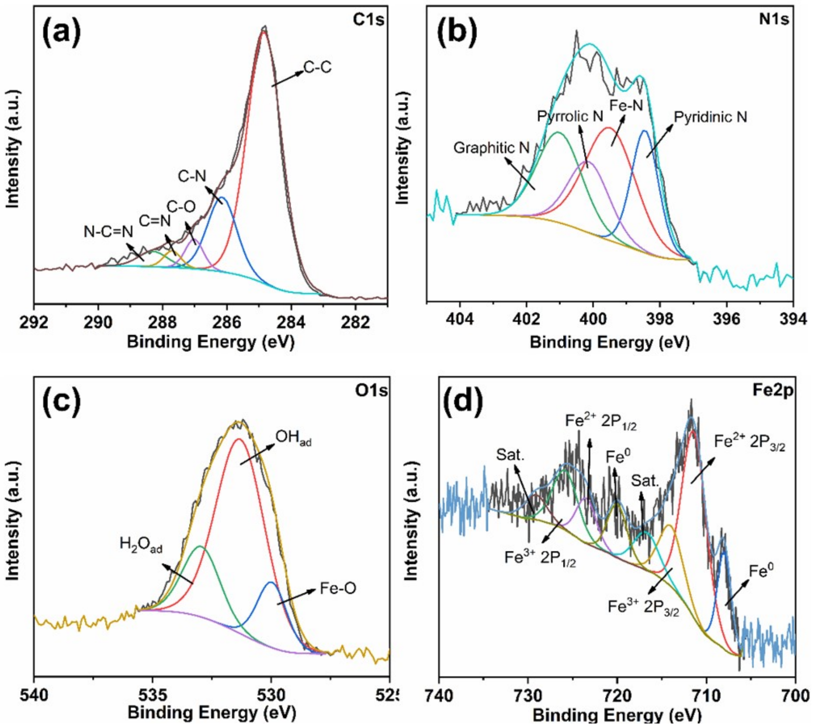

Figure S8. XPS (a) C 1s, (b) N 1s, (c) O 1s, and (d) Fe 2p of Fe_3O_4@TNC-AE.

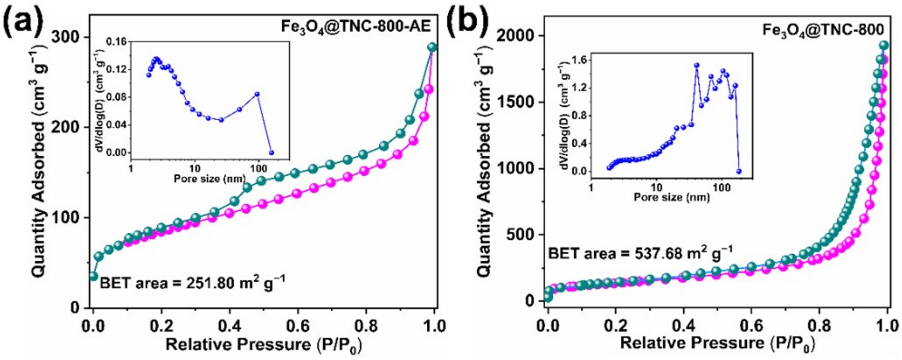

Figure S9. The specific surface areas of Brunauer-Emmett-Teller (BET) and the distributions of pore size for Fe_3O_4@TNC-AE and Fe_3O_4@TNC-800.

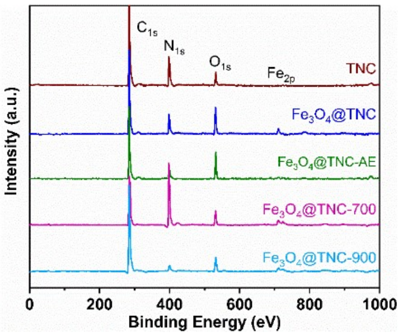

Figure S10. XPS survey spectra of TNC, Fe_3O_4@TNC, Fe_3O_4@TNC-AE, Fe_3O_4@TNC-700, and Fe_3O_4@TNC-900.

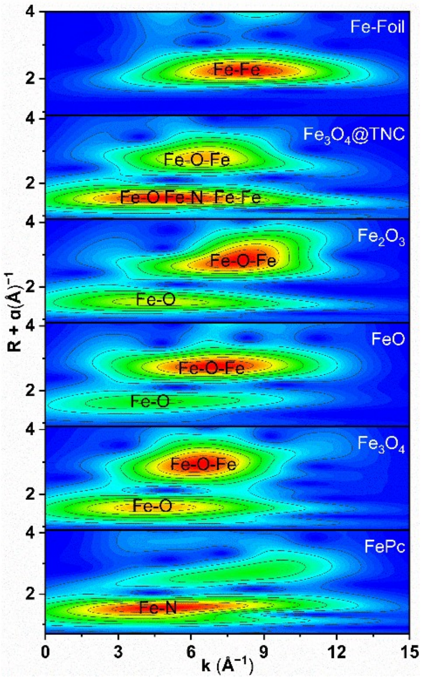

Figure S11. Wavelet transforms of the k^3-weighted EXAFS signals for Fe_3O_4@TNC and the reference samples.

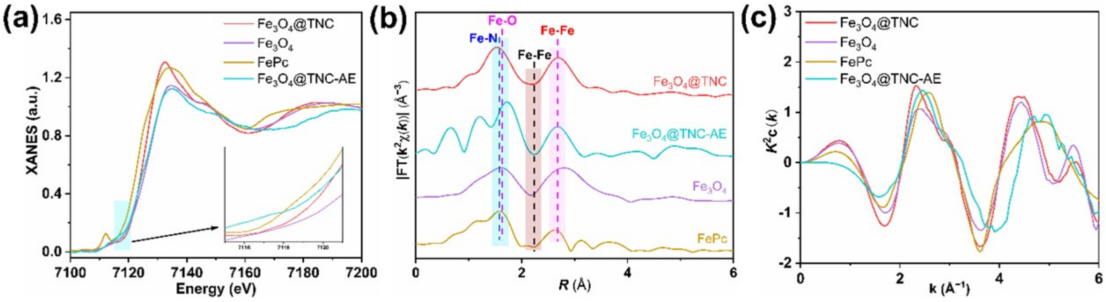

Figure S12. XANES spectra of Fe_3O_4@TNC-AE, Fe_3O_4@TNC, and the reference samples. (a) Fe K-edge XANES spectra. (b) FT k^2-weighted $\chi(k)$-a function of the EXAFS spectra of the Fe K-edge, and (c) wavelet transforms of the k^3-weighted EXAFS signals.

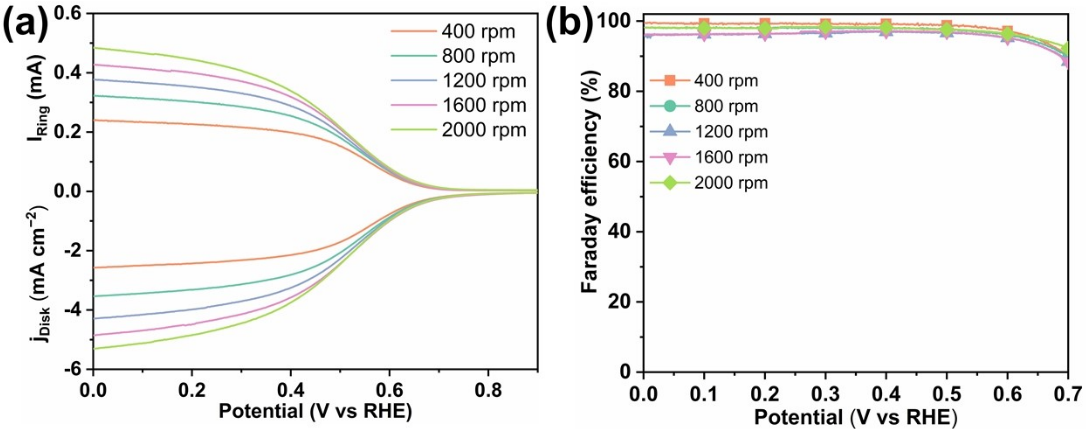

Figure S13. The effect of the rotating rate for ORR performance of Fe_3O_4@TNC. Polarization curves of Fe_3O_4@TNC in O_2-saturated 0.1 M $LiClO_4$ with a different rotating rate, the oxidation potential of 1.2 V sweep number of 5 mV/s, and the calculated Faradaic efficiency.

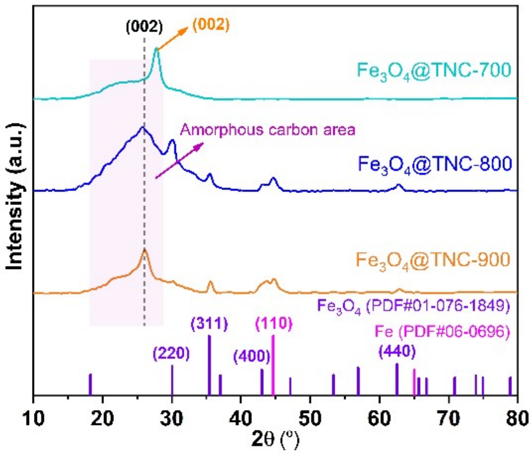

Figure S14. XRD pattern of Fe_3O_4@TNC-700, Fe_3O_4@TNC-800, and Fe_3O_4@TNC-900

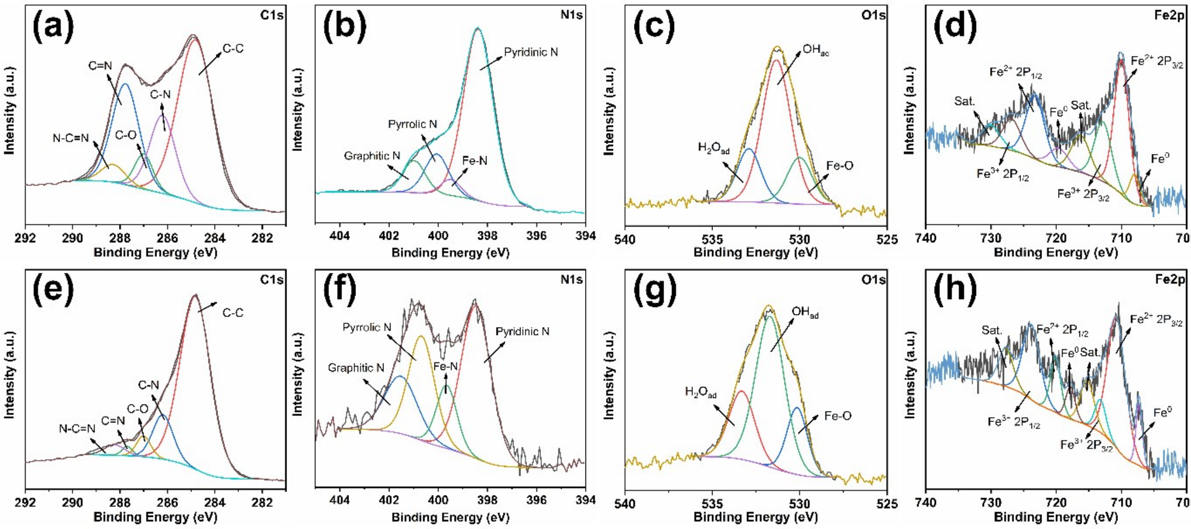

Figure S15. XPS of Fe_3O_4@TNC-700 and Fe_3O_4@TNC-900. (a) C 1s, (b) N 1s, (c) O 1s, and (d)

Fe 2p of Fe_3O_4@TNC-700. (e) C 1s, (f) N 1s, (g) O 1s, and (h) Fe 2p of Fe_3O_4@TNC-900.

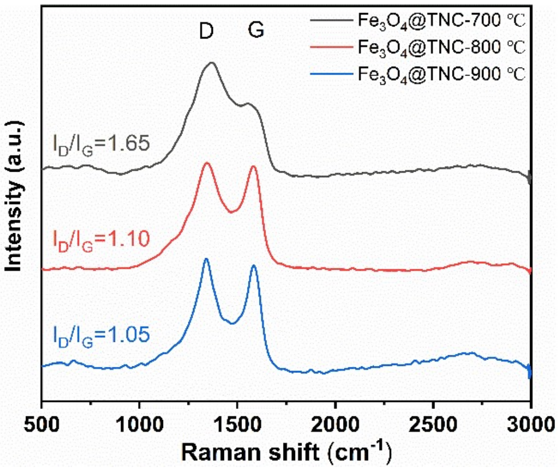

Figure S16. Raman spectra of Fe_3O_4@TNC-700, Fe_3O_4@TNC-800, and Fe_3O_4@TNC-900.

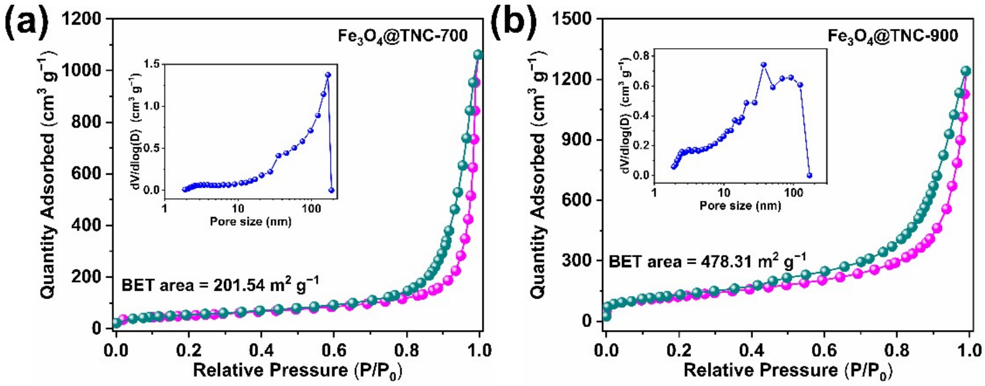

Figure S17. Porous structure. The specific surface areas of Brunauer-Emmett-Teller (BET) and the distribution of pore size for Fe_3O_4@TNC-700 and Fe_3O_4@TNC-900.

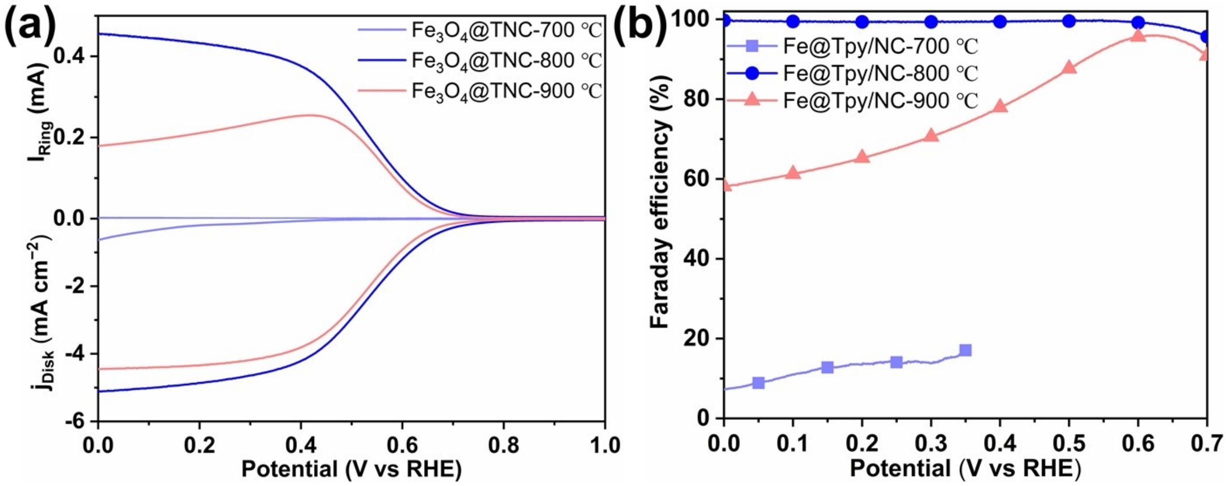

Figure S18. The effect of the pyrolysis temperature of the preparation of Fe_3O_4@TNC for ORR performance. Polarization curves and the calculated Faradaic efficiency of Fe_3O_4@TNC-700, Fe_3O_4@TNC-800, and Fe_3O_4@TNC-900.

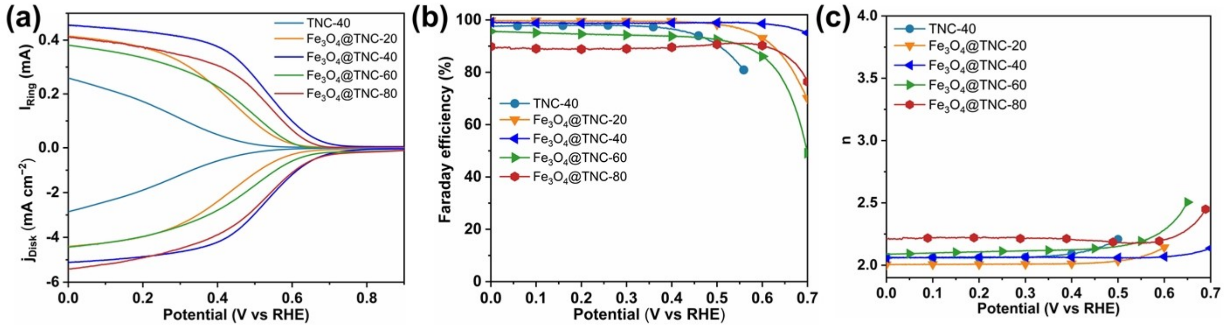

Figure S19. The effect of g-C_3N_4 usage for the preparation of Fe_3O_4@TNC samples on 2e$^-$-ORR performance. (a) Polarization curves, (b) the Faradaic efficiency of H_2O_2, and (c) the calculated transfer electron numbers of the as-prepared Fe_3O_4@TNC samples.

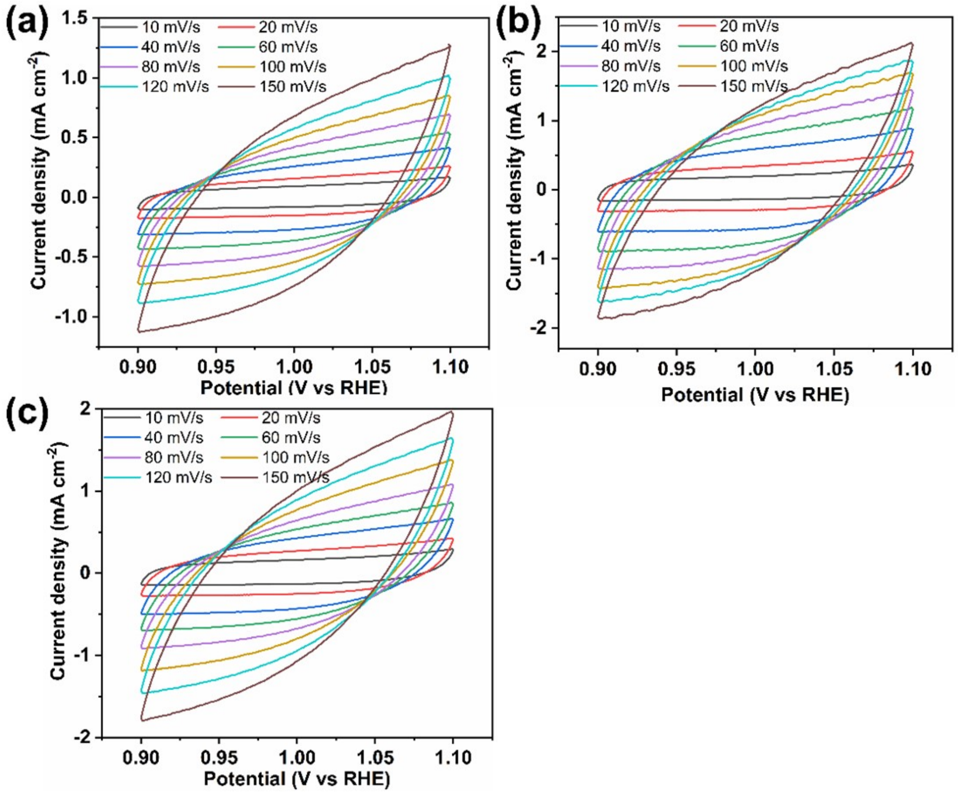

Figure S20. Determination of the C_{dl}. Cyclic voltammetry (CV) curves of (a) TNC, (b) Fe_3O_4@TNC, and Fe_3O_4@TNC-AE

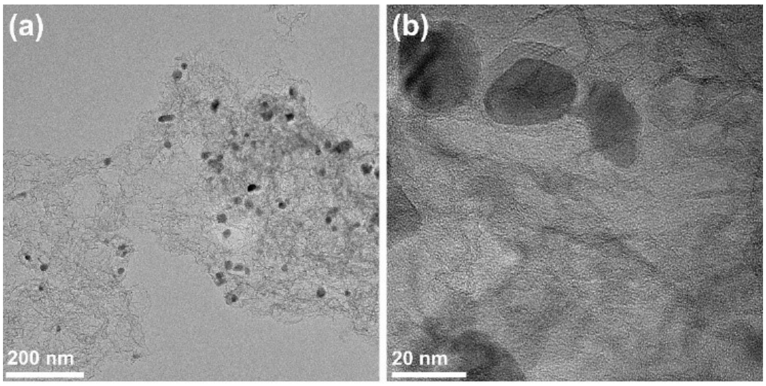

Figure S21. TEM images of Fe_3O_4@TNC after reaction

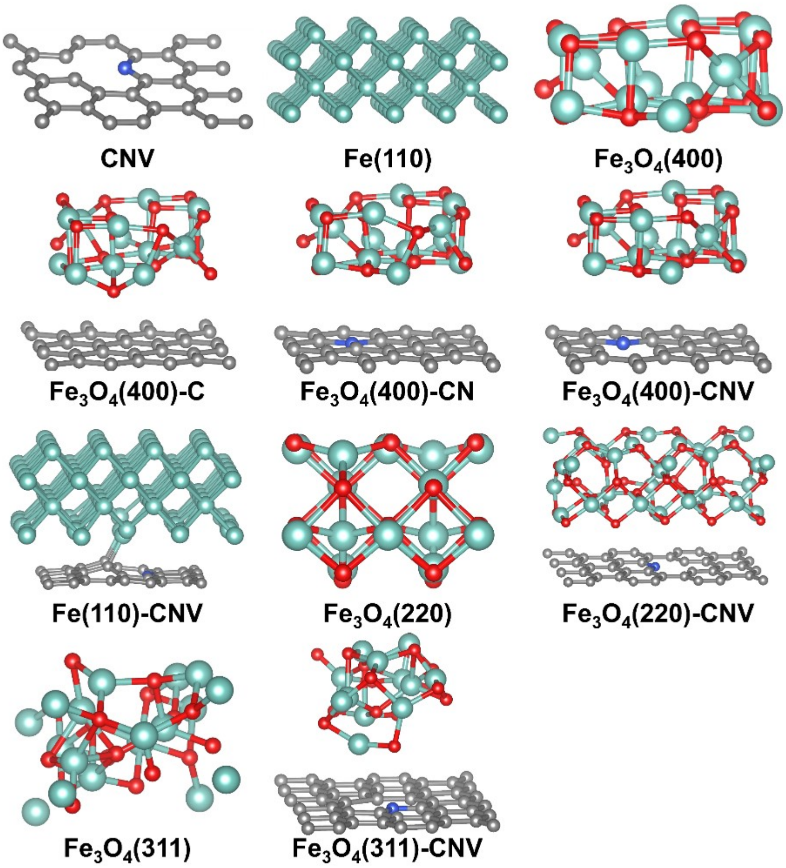

Figure S22. The optimized configuration for both Fe-based components- and carbon matrix-relevant models

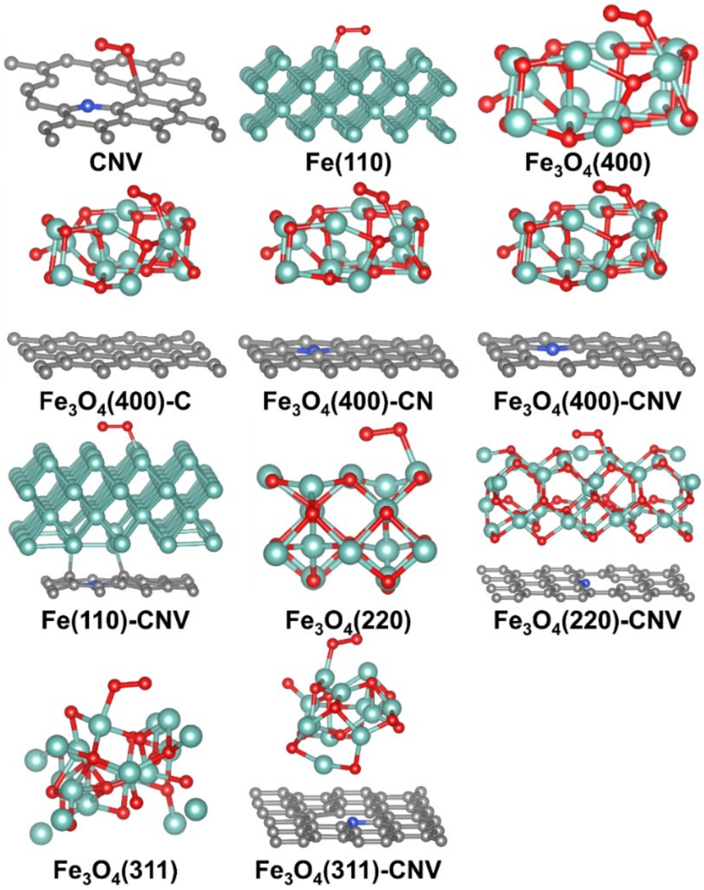

CNV Fe(110) $Fe_3O_4(400)$

$Fe_3O_4(400)$-C $Fe_3O_4(400)$-CN $Fe_3O_4(400)$-CNV

Fe(110)-CNV $Fe_3O_4(220)$ $Fe_3O_4(220)$-CNV

$Fe_3O_4(311)$ $Fe_3O_4(311)$-CNV

Figure S23. The optimized adsorption configuration of O_2 on both Fe-based components- and carbon matrix-relevant models

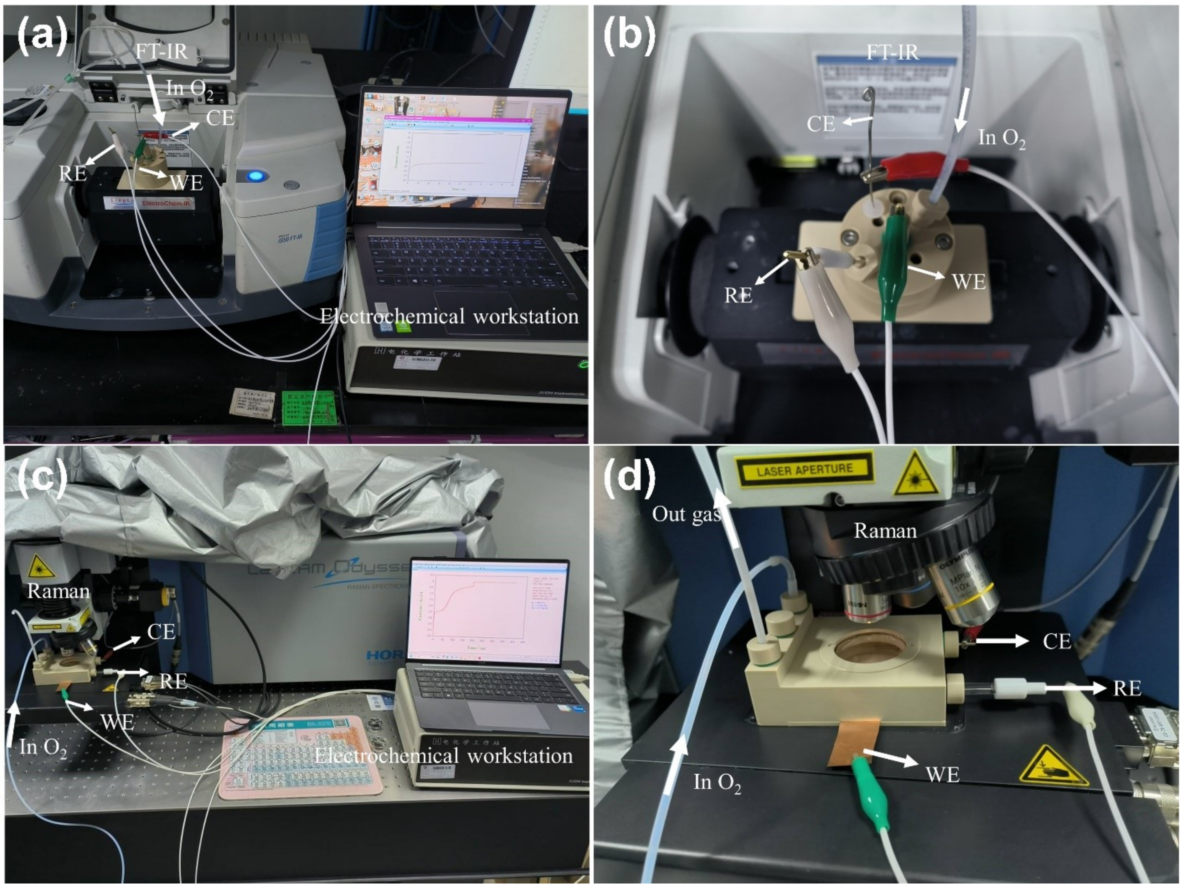

Figure S24. The experimental setup for (a) and (b) in-situ attenuated total reflectance Fourier-transform infrared (ATR-FTIR) spectroscopy and (c) and (d) in situ electrochemical Raman measurements.

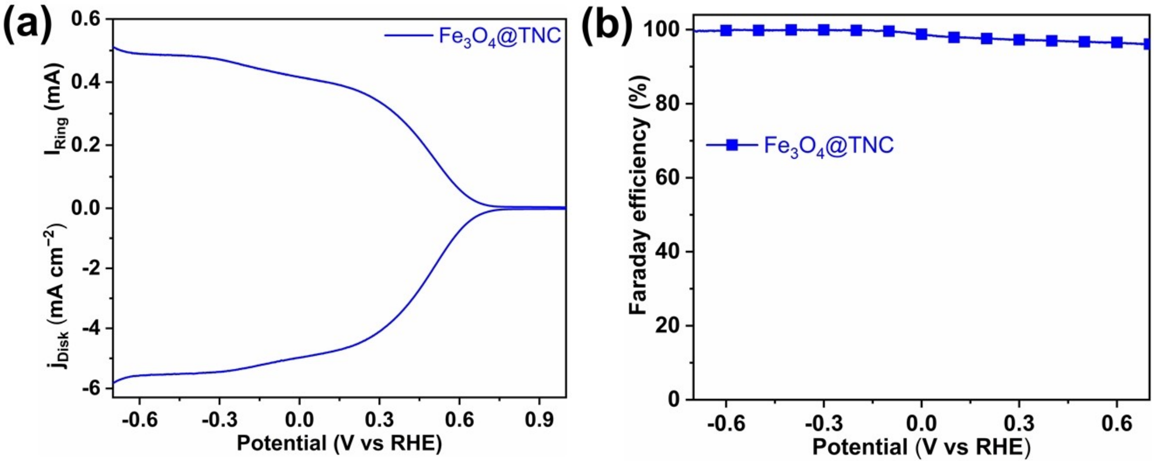

Figure S25. Evaluation of electrocatalysts for H_2O_2 production by RRDE. (a) Polarization curves of Fe_3O_4@TNC at 1600 rpm with a scan rate of 5 mV s^{-1} in O_2-saturated electrolyte containing 0.1 M $LiClO_4$ at the potential range from 0.9 to −0.7 V vs RHE and the ring electrode at a constant potential of 1.2 V, including disk current density (j_{disk}) and ring current (I_{ring}). (b) H_2O_2 Faradaic efficiency.

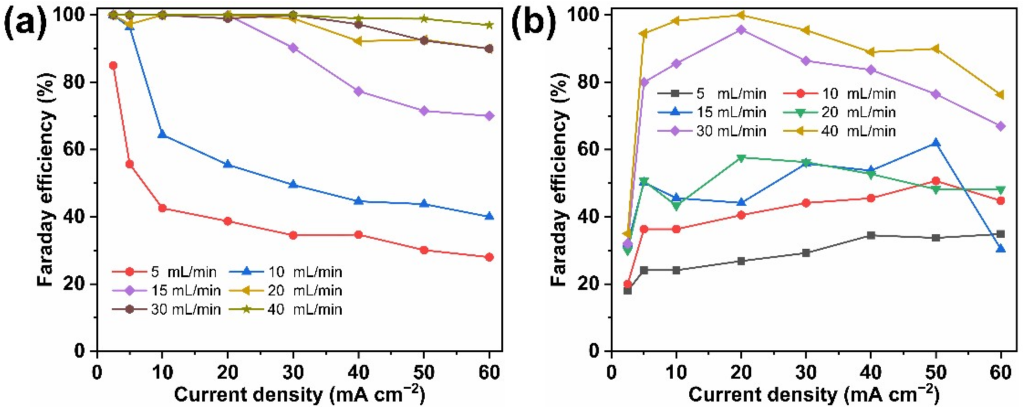

Figure S26. The effect of catalyst loading amount and water flow rate at the different current densities for neutral H_2O_2 electrosynthesis. (a) H_2O_2 Faradaic efficiency at the range of current density from 2.5 to 60 mA cm^{-2} using various flow rates of DI water and catalyst loading of 0.1 mg cm^{-2}. (b) H_2O_2 Faradaic efficiency at the range of current density from 2.5 to 60 mA cm^{-2} using various flow rates of DI water and catalyst loading of 0.3 mg cm^{-2}.

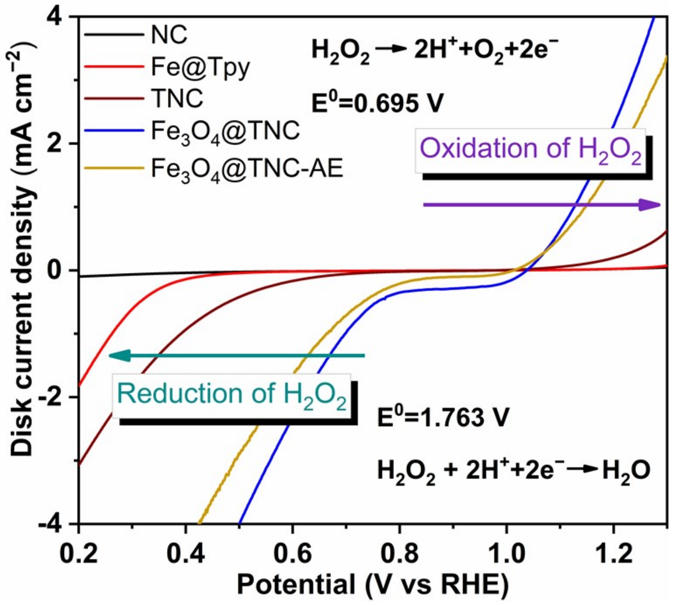

Figure S27. LSV curves of the NC, Fe@Tpy, TNC, Fe_3O_4@TNC and Fe_3O_4@TNC-AE in N_2 saturated electrolyte containing 0.1 M $LiClO_4$ and 0.1 M H_2O_2.

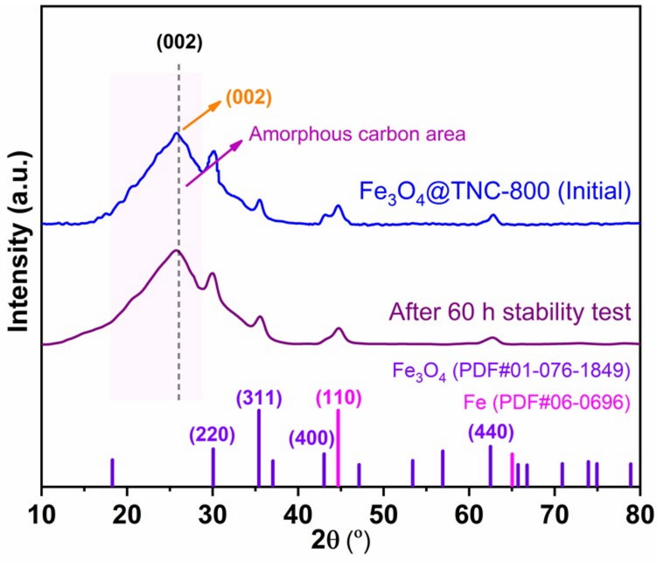

Figure S28. XRD pattern of Fe_3O_4@TNC-800 at before and after 60 h stability test.

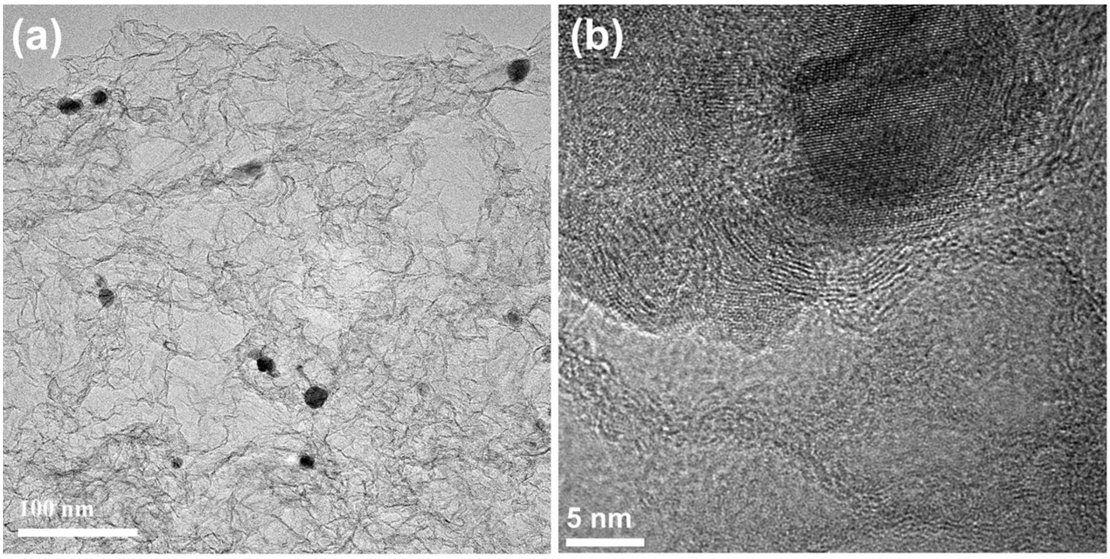

Figure S29. TEM images of Fe_3O_4@TNC after the electrolysis of 60 h in SE cell.

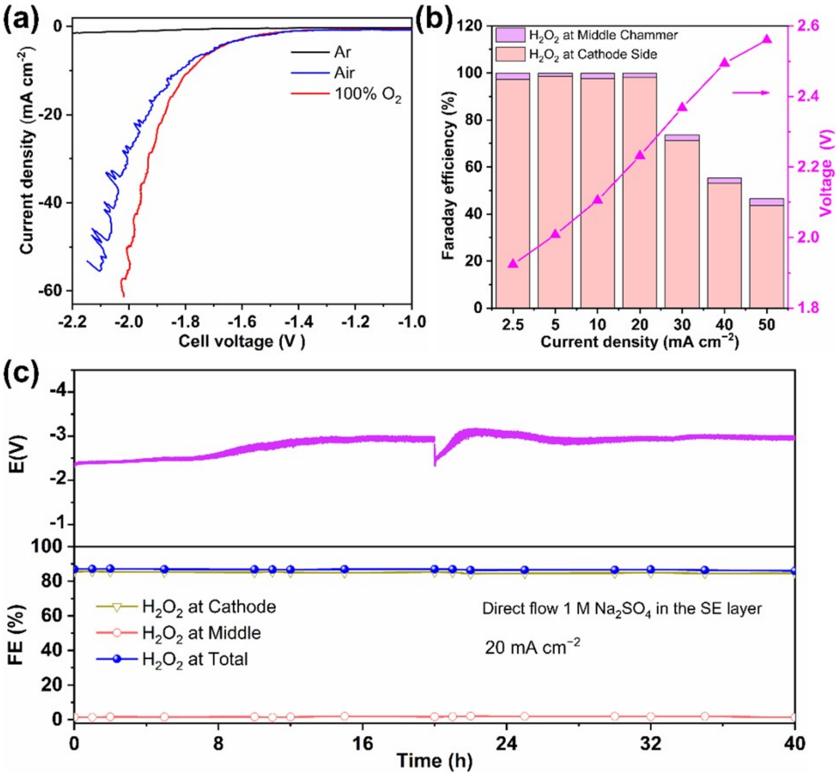

Figure S30. (a) Polarization curves using Ar, air, and O_2 as feeding gas. (b) The I-V curve and corresponding FEs use air as feeding gas for generating H_2O_2 in the middle chamber and cathode. (c) Galvanostatic stability test using air as feeding gas by directly flowing 1 M Na_2SO_4 solution in the middle chamber at 20 mA cm^{-2} current density.

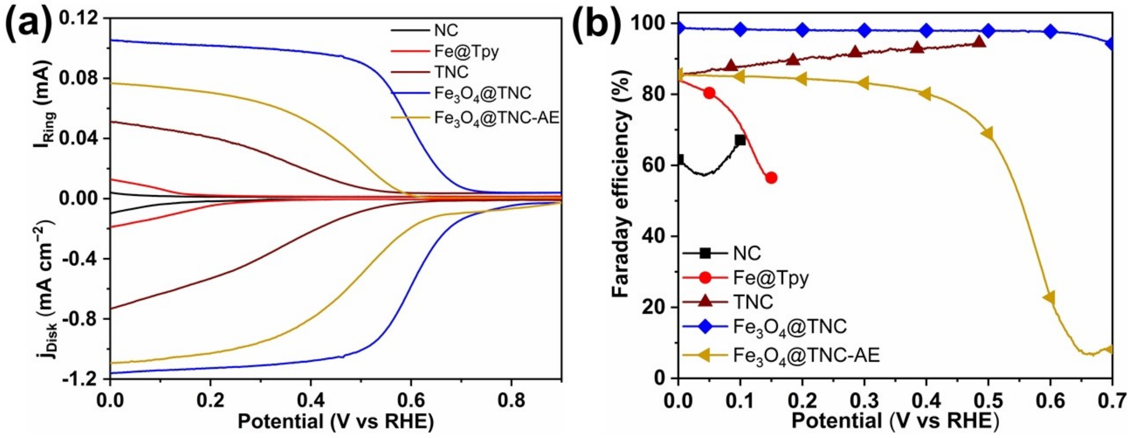

Figure S31. (a) Polarization curves were recorded at 1600 rpm with a scan rate of 5 mV s^{-1} in an Air-saturated electrolyte containing 0.1 M $LiClO_4$ and the ring electrode at a constant potential of 1.2 V, including disk current density (j_{disk}) and ring current (I_{ring}). (b) H_2O_2 Faradaic efficiency

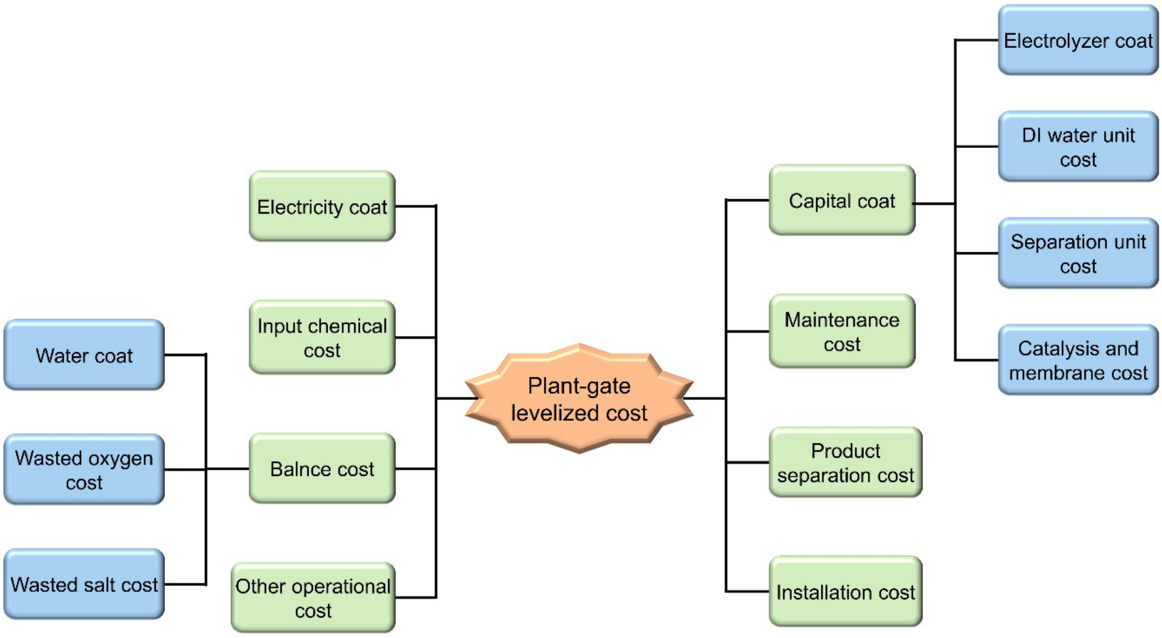

Figure S32. Model used for the techno-economic and energy evaluation of H_2O_2 electrosynthesis from O_2 and H_2O using electricity. Final H_2O_2 product concentration of 30wt% is assumed and H_2O_2 concentration and purification cost are also included. See **supplementary notes 1 and 2** for detailed information.

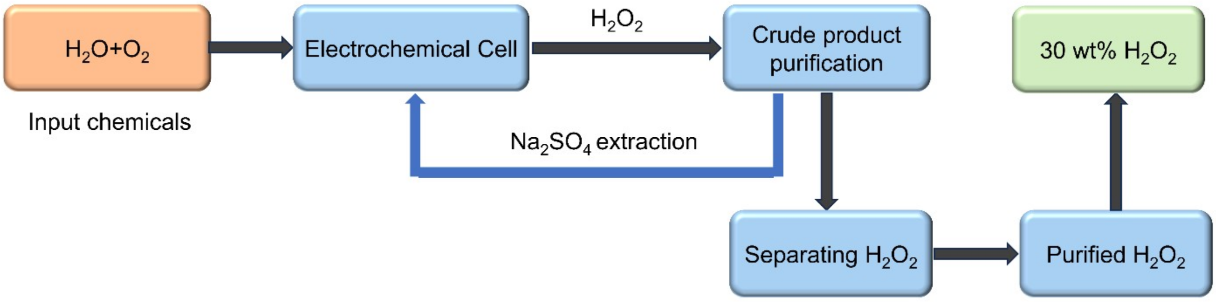

Figure S33. Processes used for techno-economic energy evaluation of H_2O_2 electrosynthesis from O_2 and H_2O using Fe_3O_4@TNC catalysts and electricity. Final H_2O_2 product concentration of 30wt% is assumed and H_2O_2 concentration and purification cost are also included. See **supplementary notes 1 and 2** for detailed information.

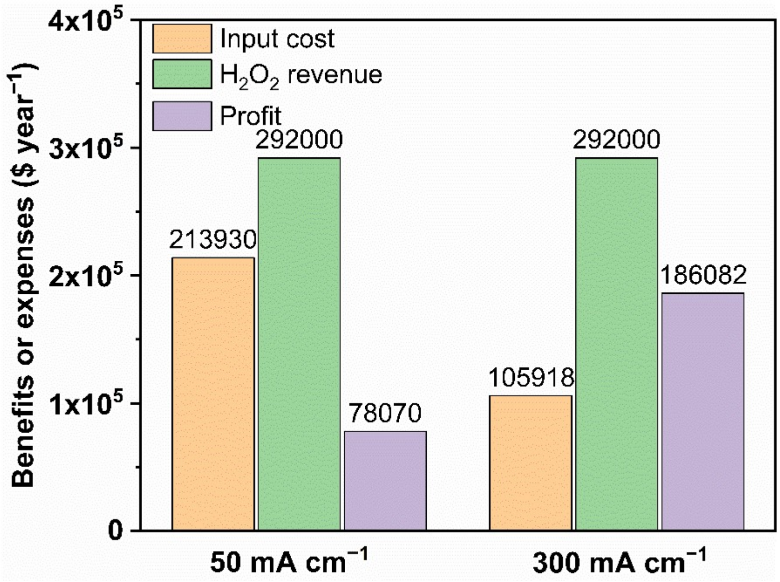

Figure S34. H_2O_2 revenue and the corresponding input cost with different conditions in SE cell.

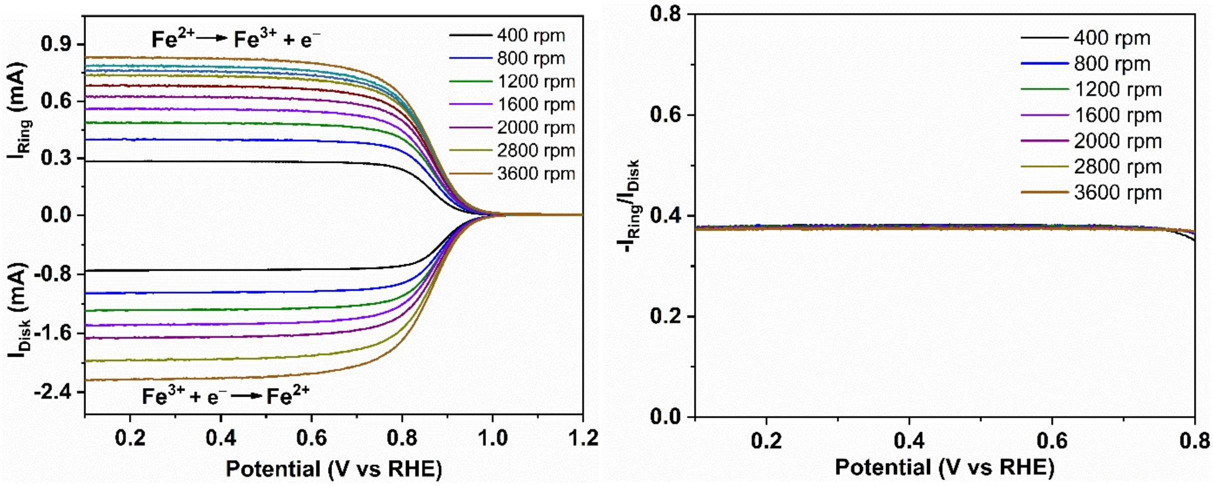

Figure S35. Calibration of the collection efficiency (N) of the RRDE by the redox of potassium ferricyanide.

Supplementary Note 1

Assumptions for techno-economic & energy analysis

We performed a technoeconomic& energy analysis to determine the feasibility of H_2O_2 production from O_2 using renewable electricity based on Ref. 1 and 2. Figure S32 shows the model used to calculate the plant-gate levelized cost of H_2O_2 from O_2 per ton of product.

A list of assumptions is as follows:

1. The production capacity of the plant is 1 ton of H_2O_2 with purity of 30wt%
2. The cost of catalysts and membrane is 2000 $\$/m^2$.
3. The electrolyzer cost was assumed 15000 $\$/m^2$.
   Electrolyzer's lifespan is 20 years.
4. The upper bound for the price of renewable electricity is 10 ¢/kWh
5. Estimation of separation cost for H_2O_2 based on vacuum distillation[1, 2]. The energy analysis of the separation is calculated based on the same separation system.
6. Other operating costs are 30% of electricity, representing additional operating costs related to operating the factory, such as labor.
7. Assuming that the power plant operates 24 hours a day, the capacity factor is 0.9.
8. Maintenance cost is 10 % of the capital cost.
9. The balance of the plant is 30 % of the total capital cost.
10. The installation cost is calculated as 10% of the total investment cost.
11. The input material price is listed below:
    - 40000 $ of capital cost 4000 $/year of operation cost for DI water production.
    - The oxygen price is 35 $/Mt[3].
    - Assuming H_2O_2 separation and enrichment, the H_2O_2 of the salt requires 1 $/Mt.
    - Na_2SO_4 price is 40 $/Mt, assuming the concentration of the configured salt solution is 1 M.
12. The market price for hydrogen peroxide is 800 $/Mt H_2O_2 on a 30% weight H_2O_2 basis.

Supplementary Note 2

Cost components of techno-economic analysis

$$\text{Total surface area needed}\left(\text{m}^2\right)=\frac{\text{Total current needed (A)}}{\text{Current density}\left(\text{A/m}^2\right)}$$

Total current needed(A)

$$= \frac{\text{Plant capacity (ton/day)} \times 10^{6} \times Mass\ of\ H_2O_2(wt\%) \times 10^{-2} \times \text{n(2)} \times \text{F (C/mol)}}{\text{Product molar mass (g/mol)} \times 24\ \text{(h/day)} \times 3600\ \text{(s/h)} \times \text{FE (\%)}}$$

$$Electrolyzere\ cost\ (\$/ton) = \frac{\text{Total surface area needed } (m^2) \times Electrolyzere\ cos}{\text{Capacity factor} \times \text{Electrolyzer lifetime(year)} \times 365\text{(day/year)} \times \text{Produ}}$$

Electricity consumption(KWh/ton)

$$= \frac{\text{Total current needed } (A) \times Cell\ voltage\ (V) \times 24\ \text{(h/day)}}{\text{Plant capacity} \times 1000\text{(W/kW)}}$$

Electricity cost($/ton)

$$= Electrolyzere\ consumption(kWh/ton) \times Electricitycost(\$/kWh)$$

Table S1. XPS or ICP-OES elemental quantification of Tpy, C_3N_4, Fe@Tpy, TNC, Fe_3O_4@TNC, Fe_3O_4@TNC-AE, Fe_3O_4@TNC-700 and Fe_3O_4@TNC-900.

Sample	C (at%)	N (at%)	O (at%)	Fe (at%) (XPS)	Fe (wt%) (XPS)	Fe (wt%) (ICP-OES)
Tpy	83.52	12.57	3.91	–	–	–
g-C_3N_4	50.71	49.29	–	–	–	–
Fe@Tpy	80.24	11.7	6.15	1.92	8.07	–
TNC	75.17	19.71	5.12	–	–	–
Fe_3O_4@TNC	73.03	13.46	11.41	2.1	8.62	11.01
Fe_3O_4@TNC-AE	76.31	9.17	13.61	0.91	4.88	7.97
Fe_3O_4@TNC-700	55.32	36.81	6.4	1.48	6.07	–
Fe_3O_4@TNC-900	86.72	4.76	7.32	1.2	5.20	–

Table S2. The detailed XPS fitting parameters of C 1s and N 1s XPS spectra of Tpy, C_3N_4, Fe@Tpy, TNC, Fe_3O_4@TNC, Fe_3O_4@TNC-AE, Fe_3O_4@TNC-700 and Fe_3O_4@TNC-900.

Species		Tpy	g-C_3N_4	Fe@Tpy	TNC	Fe_3O_4@TNC	Fe_3O_4@TNC-AE	Fe_3O_4@TNC-700	Fe_3O_4@TNC-900
C-C	Position	284.8	284.8	284.8	284.8	284.8	284.8	284.8	284.8
	Ratio	83.12%	67.7%	81.19%	76.83%	76.83%	71.40%	50.06%	77.84%
C-N	Position	285.6	286.4	285.7	286.3	286.2	286.3	286.2	286.2
	Ratio	9.89%	5.3%	8.44%	19.01%	19.01%	18.01%	17.21%	13.19%
C-O	Position	----	----	287.0	----	287.0	287.0	287.0	287.0
	Ratio	----	----	1.51%	----	3.20%	4.45%	5.55%	4.35%
C=N	Position	286.3	----	286.2	287.9	287.9	287.9	287.8	287.8
	Ratio	6.99%	----	8.87%	2.03%	2.51%	2.41%	23.50%	1.44%
N-C=N	Position	----	288.2	----	288.6	288.2	288.2	288.2	288.2
	Ratio	----	27.00%	----	2.13%	2.09%	3.73%	3.68%	3.17%
Pyridinic-N	Position	398.4	398.4	398.4	398.4	398.4	398.4	398.4	398.4
	Ratio	100.00%	77.52%	100.00%	56.93%	56.94%	20.65%	71.49%	47.86%
Fe-N	Position	----	----	----	----	399.5	399.5	399.5	399.5
	Ratio	----	----	----	----	35.84%	35.84%	4.71%	13.46%
Pyrrolic-N	Position	----	400.1	----	400.1	400.1	400.1	400.1	400.1
	Ratio	----	17.23%	----	19.25%	18.17%	18.19%	13.55%	22.84%
Graphitic-N	Position	----	401.2	----	401.2	401.2	401.2	401.2	401.2
	Ratio	----	5.25%	----	25.82%	19.05%	25.32%	10.25%	15.84%

Table S3. Brunauer-Emmett-Teller (BET) Surface Analysis Results

Sample	Specific surface area (m^2/g)	Pore Width (nm)
Fe_3O_4@TNC-700	201.54	29.66
Fe_3O_4@TNC-800	537.68	22.18
Fe_3O_4@TNC-900	478.31	16.00
Fe_3O_4@TNC-AE	251.80	6.12

Table S4. C_{dl} and corresponding ECSA of TNC, Fe_3O_4@TNC, and Fe_3O_4@TNC-AE

Sample	C_{dl} (mF cm^{-2})	ECSA (cm^2 cm^{-2} $_{electrode}$)
TNC	4.6	115.0
Fe_3N_4@TNC	11.1	277.5
Fe_3N_4@TNC-AE	6.7	167.5

Table S5. Summary of the electrocatalysts for H_2O_2 production via neutral ORR in Figure 2i.

Catalyst	**Electrolyte**	**Onset potentials (RHE)**	**Selectivity and potential at $J_{k, H2O2}$ = 2 mA/cm$^2_{disk}$**	**H_2O_2 yield（mol $g_{catal.}^{-1}$ h^{-1}）and FE (%)**	**Stability test**	**Ref.**
Fe_3O_4@TNC	0.1 M $LiClO_4$	0.75	97%@0.55	8.89@87.0%	60 h	This work
CoPC-CNT(O)	0.1 M K_2SO_4	0.55	92%@0.40	26.1@38.0%	100 h	4
Ni-HAB	0.05 M NiPi	0.62	50%@0.43	12.9@39.5%	1.5 h	5
Pd_4Se NPs	0.1 M KCl	0.71	80%@0.57	6.0@79.2%	2 h	6
C-$CoSe_2$	0.05 M NiPi	0.75	60%@0.45	----	NA	7
CoPC-OCNT	0.1 M K_2SO_4	0.60	92@0.43	0.47@92.0%	30 h	8
MCHS	0.1 M PBS	0.61	90%@0.51	0.03@93.1%	Cycle 2500	9
Fe-CNT	0.1 M PBS	0.55	90%@0.36	----	2.5 h	10
B-C	0.1 M Na_2SO_4	0.45	78%@0.25	4.6@84.5%	NA	11
Co–SAs/NC	0.1 M Na_2SO_4	0.48	30%@0.15	0.06@90.0%	NA	12
CB600	0.1 M Na_2SO_4	0.41	77%@0.15	0.3@76.3%	0.5 h	13
MBC-2	0.05 M Na_2SO_4	0.41	80%@0.16	6.4@80.0%	6 h	14
Co-N-C	0.1 M K_2SO_4	0.61	58%@0.40	--@--	NA	15
PCMNS	0.1 M K_2SO_4	0.49	90%@0.35	1.1@80.5%	10 h	16
ZnCo-ZIF	0.1 M PBS	0.60	90%@0.05	4.30@99.0%	0.25 h	17
ZnO	0.1 M K_2SO_4	0.46	97%@0.29	3.66@98.1%	50 h	18

Co-N-C(2)	0.1 M PBS	0.78	60%@0.70	----	200 h	19
NiPyCN/CN	0.1 M K_2SO_4	0.45	80%@0.42	3.89@80.5%	90 h	20
N,O-$CNS_{0.5}$	0.1 M K_2SO_4	0.65	91%@0.41	6.71@65.0%	24 h	21
Pd/MCS-8	0.1 M K_2SO_4	0.68	95%@0.51	15.77@86.0%	24 h	22
CoPc-6wt%/o-SWCNT-2	0.1 M K_2SO_4	0.48	94%@0.31	5.85@84.5%	75 h	23
CoNCB	0.1 M PBS	0.76	96%@0.60	4.72@60.0%	5 h	24
$PdSe_2$	0.05 M NaPi	0.61	70%@0.19	----	48 h	25
CBNO	0.1 M Na_2SO_4	0.67	87%@0.21	13.4@95%	25 h	26

Table S6. The (220), (311), (400), and (440) crystal plane ratios of Fe_3O_4 in Fe_3O_4@TNC, Fe_3O_4@TNC-AE, Fe_3O_4@TNC-700, Fe_3O_4@TNC-900 and Fe_3N_4@TNC (After 60 h stability test) were determined by XRD data.

Sample	(220)	(311)	(400)	(440)
Fe_3N_4@TNC	59.9%	19.5%	14.2%	6.4%
Fe_3N_4@TNC-AE	6.0 %	49.7%	23.5%	20.8%
Fe_3N_4@TNC-700	0%	0%	0%	0%
Fe_3N_4@TNC-900	18.0%	33.4%	36.1%	12.5%
Fe_3N_4@TNC (After 60 h)	58.9%	20.1%	10.1%	10.9%

References

1. H. Eickhoff, F. Lode, E. Arevalo, M. Brendel and C. Wallert, 2015.
2. G. Goor, J. Glenneberg and S. Jacobi, in *Ullmann's Encyclopedia of Industrial Chemistry*, 2007.
3. J. Na, B. Seo, J. Kim, C. W. Lee, H. Lee, Y. J. Hwang, B. K. Min, D. K. Lee, H. S. Oh and U. Lee, *Nat. Commun.*, 2019, **10**, 5193.
4. B.-H. Lee, H. Shin, A. S. Rasouli, H. Choubisa, P. Ou, R. Dorakhan, I. Grigioni, G. Lee, E. Shirzadi, R. K. Miao, J. Wicks, S. Park, H. S. Lee, J. Zhang, Y. Chen, Z. Chen, D. Sinton, T. Hyeon, Y.-E. Sung and E. H. Sargent, *Nat. Catal.*, 2023, **6**, 234-243.
5. R. D. Ross, H. Sheng, Y. Ding, A. N. Janes, D. Feng, J. R. Schmidt, C. U. Segre and S. Jin, *J. Am. Chem. Soc.*, 2022, **144**, 15845-15854.
6. C. Yang, S. Bai, Z. Yu, Y. Feng, B. Huang, Q. Lu, T. Wu, M. Sun, T. Zhu, C. Cheng, L. Zhang, Q. Shao and X. Huang, *Nano Energy*, 2021, **89**, 106480.
7. H. Sheng, R. D. Ross, J. R. Schmidt and S. Jin, *ACS Energy Lett.*, 2023, 8, 196-212.
8. P. Cao, X. Quan, X. Nie, K. Zhao, Y. Liu, S. Chen, H. Yu and J. G. Chen, *Nat. Commun.*, 2023, **14**, 1-12.
9. Y. Pang, K. Wang, H. Xie, Y. Sun, M.-M. Titirici and G.-L. Chai, *ACS Catal.*, 2020, **10**, 7434-7442.
10. K. Jiang, S. Back, A. J. Akey, C. Xia, Y. Hu, W. Liang, D. Schaak, E. Stavitski, J. K. Norskov, S. Siahrostami and H. Wang, *Nat. Commun.*, 2019, **10**, 3997.
11. Y. Xia, X. Zhao, C. Xia, Z. Y. Wu, P. Zhu, J. Y. T. Kim, X. Bai, G. Gao, Y. Hu, J. Zhong, Y. Liu and H. Wang, *Nat. Commun.*, 2021, **12**, 4225.
12. H. Xu, S. Zhang, J. Geng, G. Wang and H. Zhang, *Inorg. Chem. Front.*, 2021, **8**, 2829-2834.
13. H. Zhang, Y. Li, Y. Zhao, G. Li and F. Zhang, *ACS Appl. Mater. Interfaces*, 2019, **11**, 27846-27853.
14. M. Gao, Z.-Y. Wang, Y.-R. Yuan, W.-W. Li, H.-Q. Liu and T.-Y. Huang, *Chem. Eng. J.*, 2022, **434**, 134788.
15. Y. Sun, L. Silvioli, N. R. Sahraie, W. Ju, J. Li, A. Zitolo, S. Li, A. Bagger, L. Arnarson, X. Wang, T. Moeller, D. Bernsmeier, J. Rossmeisl, F. Jaouen and P. Strasser, *J. Am. Chem. Soc.* 2019, **141**, 12372-12381.

16. R. Hu, Y. Cui, B. Huang and L. Guan, *ACS Appl. Mater. Interfaces*, 2021, **13**, 35856-35864.
17. C. Zhang, L. Yuan, C. Liu, Z. Li, Y. Zou, X. Zhang, Y. Zhang, Z. Zhang, G. Wei and C. Yu, *J. Am. Chem. Soc.*, 2023, **145**, 7791-7799.
18. Y. Zhou, L. Xu, J. Wu, W. Zhu, T. He, H. Yang, H. Huang, T. Cheng, Y. Liu and Z. Kang, *Energy Environ. Sci.*, 2023, **16**, 3526-3533.
19. Y. X. Du, Q. Yang, W. T. Lu, Q. Y. Guan, F. F. Cao and G. Zhang, *Adv. Funct. Mater.*, 2023, **33**, 2300895.
20. L. Sun, X. Jin, T. Su, A. C. Fisher and X. Wang, *Adv. Mater.*, 2023, **36**, e2306336.
21. L. Jing, Q. Tian, W. Wang, X. Li, Q. Hu, H. Yang and C. He, *Adv. Energy Mater.*, 2024, **14**, 2304418.
22. L. Jing, W. Wang, Q. Tian, Y. Kong, X. Ye, H. Yang, Q. Hu and C. He, *Angew. Chem. Int. Ed.*, 2024, **63**, e202403023.
23. Y. Li, H. Cheng, M. Wang, J. Xu and L. Guan, *Mater. Horiz.*, 2024, **11**, 2517-2527.
24. L. Liu, L. Kang, J. Feng, D. G. Hopkinson, C. S. Allen, Y. Tan, H. Gu, I. Mikulska, V. Celorrio, D. Gianolio, T. Wang, L. Zhang, K. Li, J. Zhang, J. Zhu, G. Held, P. Ferrer, D. Grinter, J. Callison, M. Wilding, S. Chen, I. Parkin and G. He, *Nat. Commun.*, 2024, **15**, 4079.
25. R. D. Ross, K. Lee, G. J. Quintana Cintrón, K. Xu, H. Sheng, J. R. Schmidt and S. Jin, *J. Am. Chem. Soc.*, 2024, **146**, 15718-15729.
26. Z. Song, X. Chi, S. Dong, B. Meng, X. Yu, X. Liu, Y. Zhou and J. Wang, *Angew. Chem. Int. Ed.*, 2024, **63**, e202317267.